Use of a Rapid Cytotoxicity Screening Approach To Engineer a Safer Zinc Oxide Nanoparticle through Iron Doping

Saji George,[†,‡,○] Suman Pokhrel,[§,○] Tian Xia,[†,‡,○] Benjamin Gilbert,[⊥] Zhaoxia Ji,[‡] Marco Schowalter,[¶] Andreas Rosenauer,[¶] Robert Damoiseaux,[#,‡] Kenneth A. Bradley,[∇,‡] Lutz Mädler,[§] and André E. Nel[†,‡,*]

[†]Department of Medicine-Division of NanoMedicine, University of California, Los Angeles, California, [‡]California NanoSystems Institute at University of California, Los Angeles, California, [§]IWT Foundation Institute of Materials Science, Department of Production Engineering, University of Bremen, Germany, [⊥]Earth Sciences Division, Lawrence Berkeley National Laboratory, Berkeley, California, [¶]University of Bremen, Institute for Solid State Physics, Bremen, Germany, [#]Molecular Shared Screening Resources, University of California, Los Angeles, California, and [∇]Department of Microbiology, Immunology & Molecular Genetics, University of California, Los Angeles, California. [○]These authors contributed equally to this work.

ABSTRACT The establishment of verifiably safe nanotechnology requires the development of assessment tools to identify hazardous nanomaterial properties that could be modified to improve nanomaterial safety. While there is a lot of debate of what constitutes appropriate safety screening methods, one approach is to use the assessment of cellular injury pathways to collect knowledge about hazardous material properties that could lead to harm to humans and the environment. We demonstrate the use of a multiparameter cytotoxicity assay that evaluates toxic oxidative stress to compare the effects of titanium dioxide (TiO_2), cerium oxide (CeO_2), and zinc oxide (ZnO) nanoparticles in bronchial epithelial and macrophage cell lines. The nanoparticles were chosen on the basis of their volume of production and likelihood of spread to the environment. Among the materials, dissolution of ZnO nanoparticles and Zn^{2+} release were capable of ROS generation and activation of an integrated cytotoxic pathway that includes intracellular calcium flux, mitochondrial depolarization, and plasma membrane leakage. These responses were chosen on the basis of the compatibility of the fluorescent dyes that contemporaneously assess their response characteristics by a semiautomated epifluorescence procedure. Purposeful reduction of ZnO cytotoxicity was achieved by iron doping, which changed the material matrix to slow Zn^{2+} release. In summary, we demonstrate the utility of a rapid throughput, integrated biological oxidative stress response pathway to perform hazard ranking of a small batch of metal oxide nanoparticles, in addition to showing how this assay can be used to improve nanosafety by decreasing ZnO dissolution through Fe doping.

KEYWORDS: nanoparticle · nanotoxicology · high content screening · hazard ranking · zinc oxide · dissolution · iron doping

The widespread use of engineered nanomaterials increases the likelihood that these materials will come into contact with humans and the environment. Because many biological processes take place at the nanoscale level there is the potential that engineered nanomaterials may interact with biomolecules and cellular processes that are critical to life.[1] Thus, although nanotechnology presents immense opportunities, there are concerns about the safety of these materials following intentional and unintentional human exposures. Identification of the hazard potential of nanoparticles and preventing harm to humans and the environment is of great importance for the widespread implementation and acceptance of this technology.[1,2] Early identification of potentially hazardous nanomaterial properties could also allow the redesign of these materials to improve safety while still maintaining key nanoscale properties.[3] Such an approach has been implemented by side chain modification of nanoparticles,[3] for example, changing cationic amines to neutral acetamides on a dendrimer surface or attaching polyethylene glycol (PEG) to the particle surface to decrease bioreactivity through steric hindrance.[4] Similarly, functionalizing the fullerene and single-walled carbon nanotubes (SWNTs) with carboxyl or hydroxyl groups was reported to decrease cytotoxic potential.[5,6] However, there are not many examples where the basic material characteristics have been modified through a rational design process to ameliorate toxicity. This is in part due to the lack of understanding of the material properties and the biological mechanisms that lead to toxicity, including how to properly screen for nanomaterial hazard. Hence, it has been difficult to implement a rational approach for the safe design of nanomaterials.

A screening tool that is capable of rapidly assessing key signals of nanoparticle toxicity in reporter cells would enhance the efficiency and rate at which hazard profiles can be acquired to plan *in vivo* testing as well as for the identification of hazardous material properties that could be re-engineered during the design phase.[7] Rapid throughput screening approaches include the use of fluorescence-based cellular

*Address correspondence to anel@mednet.ucla.edu.

Received for review October 27, 2009 and accepted December 17, 2009.

Published online December 31, 2009.
10.1021/nn901503q

assays with automated read-out by epifluorescence microscopy. These approaches can also be combined with high content screening (HCS), which has facilitated understanding of biological phenomena in cells as well as in drug screening.[8] Recently, rapid throughput multiparametric cellular screening has also been shown to be useful as a toxicological screening tool.[9−12] The adoption of rapid throughput procedures would permit batches of nanomaterials or nanomaterial libraries to be screened for cytotoxic potential.[12,13] This could speed up knowledge acquisition of the property−activity relationships that are required to understand nanomaterial hazard at the nano−bio-interface.[3]

Here, we report the optimization and validation of a multiparametric fluorescence assay to compare the cytotoxicity of metal oxide nanoparticles (TiO_2, CeO_2 and ZnO), differing in their ability to generate oxidant injury in mammalian cells.[1,14,15] We also show that this assay can be used for the identification of a hazardous nanomaterial property that could be improved through iron doping. We used oxidative stress injury to develop our assay based on previous demonstration that a hierarchical oxidative stress model is a useful screening procedure for nanoparticles that are capable of oxygen radical generation (Supporting Information, Figure S1).[1] Moreover, we have also previously shown that the hierarchical oxidative stress paradigm is relevant for *in vitro* profiling of ambient particulate matter and is able to predict the ability of ambient ultrafine particles to induce atherosclerotic plaque formation and allergic airway inflammation in animals.[16,17] Briefly, Tier 1 oxidative stress constitutes a protective response wherein phase II enzyme expression attempts to restore redox disequilibrium.[1,14,18,19] However, if this antioxidant defense mechanism is overwhelmed, further escalation of oxidative stress could trigger a Tier 2 response that is characterized by pro-inflammatory effects resulting from cytokine and chemokine production.[14,16,17] The highest tier of oxidative stress (Tier 3), aka toxic oxidative stress, involves mitochondrion-mediated cytotoxicity that can be triggered through intracellular calcium ($[Ca^{2+}]_i$) flux and opening of the mitochondrial permeability transition pore.[20] We have previously demonstrated that a series of assays that assess each tier of oxidative stress can be used for *in vitro* hazard ranking of pro-oxidative nanoparticles.[15] However, because of the labor intensiveness and longer time to complete these assays, we set out to develop a multiparametric assay that utilizes fluorescence read-out of an integrated set of oxidative stress responses in one sitting. We show that it was possible to achieve this integration by combining oxidative stress events at the highest level of oxidative stress (Tier 3). Following the validation and optimization of our rapid throughput screening procedure, we theorized that it should be possible to demonstrate that the modification of a key ZnO property involved in oxidative injury, namely particle dissolution, could lead to a reduction in injury. We demonstrate that for ZnO nanoparticles it was possible to employ iron doping to change the dissolution characteristics and thereby render a less toxic material in our multiparametric screen.

RESULTS

Metal Oxide Nanoparticle Synthesis and Characterization. TiO_2, CeO_2, and ZnO nanoparticles were synthesized by flame spray pyrolysis (FSP) as described in Materials and Methods. The choice of these materials to optimize and demonstrate the usefulness of rapid screening procedure was based on our recent demonstration of their differential toxic effects in cellular screening assays that assess biological hazard through incremental levels of oxidant injury.[14,15] The TEM image of TiO_2 revealed tightly packed aggregates of small spherical (~10 nm) nanocrystals (Figure 1A,a). The corresponding wide spot selected area electron diffraction (SAED) pattern (Figure 1A,d) is indicative of the high crystallinity of TiO_2.[21] The XRD patterns show that the crystallites were either anatase or rutile with the approximate ratio of 4:1 (Figure 1B,a). The intense diffraction peaks at (101), (004), (200), (105), (204) are attributed to anatase while those at (110) and $2\theta \approx 75.24$ (101) represent the rutile phase.[22−24] FSP synthesis of CeO_2 from a cerium 2-ethylhexanoate precursor yielded particles of approximate size 5−8 nm (Figure 1A,b). Their SAED pattern shows typical crystalline dots, which imply that the particles are composed of many small crystals attached to each other in the same orientation to yield polycrystals (Figure 1A,e).[25] The XRD pattern showing CeO_2 planes at (111), (200), (220), (311), (222), (400), (311), (420), and (422) are indexed to the FCC structure with space group *Fm*3*m*, having a lattice constant of $a = 0.5410$ nm according to JCPDS 78-0694 (Figure 1B,b).[26−29]

TEM images showed that 20 nm spheroidal ZnO particles that exhibit high crystallinity occasionally formed broken rodlike structures of 15−20 nm (Figure 1A, c). The SAED rings confirm that ZnO nanocrystals are in the wurtzite phase[30] and exhibit preferential instead of random orientation (Figure 1A,f). All peaks in the XRD pattern for ZnO were indexed to hexagonal single phase ZnO (JCPDS No. 36-1451, $a = b = 3.2498$ Å, $c = 5.2066$ Å, space group: *P*63*mc*)[31−34] in which each zinc atom is tetrahedrally coordinated with four oxygen atoms (Figure 1B,c). Peaks at $2\theta = 31.8°$, 34.5°, and 36.5° are attributed to ZnO (100), (002), and (10 1) planes, respectively.

Since the surface chemistry and dispersion state of the nanoparticles affect cellular uptake and bioreactivity, we used a protein stabilization strategy to properly disperse the metal oxide nanoparticles in biological tissue culture media. Tissue culture media we used include bronchial epithelial growth medium (BEGM) and complete Dulbecco's modified eagle's medium (CD-

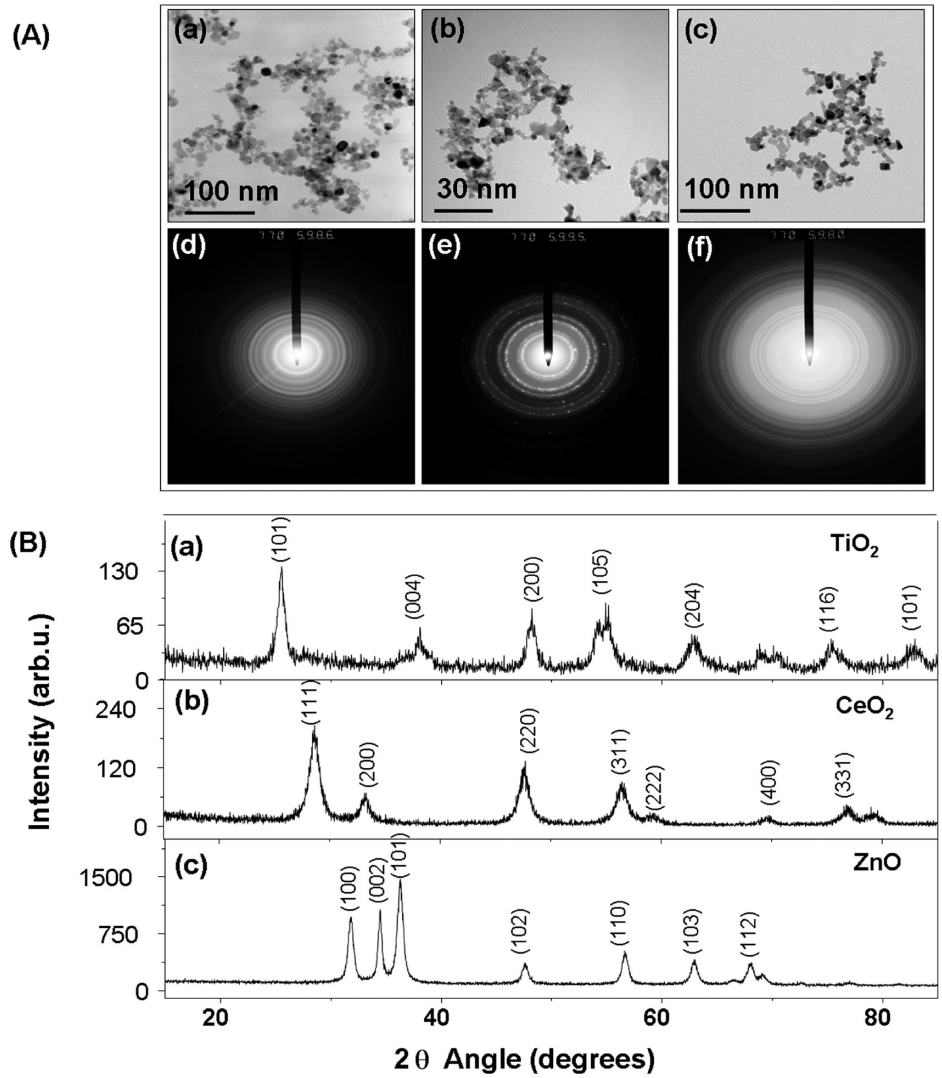

Figure 1. Physicochemical characterization of metal oxide nanoparticles (NPs). (A) TEM characterization of the NPs used in this study: (a) TiO_2, (b) CeO_2, (c) ZnO; and SAED of (d) TiO_2, (e) CeO_2, and (f) ZnO NPs. All NPs were prepared and applied to grids as described in the synthesis and experimental section. (B) XRD patterns of TiO_2, CeO_2, and ZnO (metal oxide) NPs.

MEM) for growing bronchial epithelial (BEAS-2B) and macrophage (RAW 264.7) cell lines, respectively.[15] Our approach is to initially disperse the particles in deionized water (to avoid buffered salt effects), and then to stabilize the particles by protein addition before final transfer into the tissue culture media. Table 1 shows that particles agglomerate as a result of the buffered salts in the culture media.[35] However, the agglomeration size was significantly reduced when BSA at a concentration of 20 mg/mL (w/v) was used to stabilize the nanoparticles before transfer to BEGM containing 2 mg/mL BSA or DMEM containing 10% fetal bovine serum (FBS). BSA is known to transiently adsorb to metal oxide surfaces[36] and stabilize particle dispersion through steric or electrosteric effects. Upon dispersing the nanoparticles in cell culture media, their original

TABLE 1. NP Size and Zeta-Potential in Experimental Dispersion Conditions[a]

	size (nm)[b]						zeta potential (mV)		
NPs	water	BEGM	BEGM+BSA	BSA-coated NPs in BEGM+BSA	CDMEM	BSA-coated NPs in CDMEM	water	BSA-coated NPs in BEGM+BSA	BSA-coated NPs in CDMEM
TiO_2	687	791.4	166.75	131.5	114.75	115.1	3.89	−9.58	−9.95
CeO_2	281.9	1633	498.5	320.15	131.8	137.05	10.7	−8.83	−8.33
ZnO	145.5	186.2	84.3	45.17	24.23	28.86	17.4	−7.16	−7.93

[a]Particle size and zeta potential in solution were measured by ZetaSizer Nano (Malvern). CDMEM = complete Dulbecco's modified eagle media, which contains 10% fetal bovine serum (FBS). BEGM = bronchial epithelial growth medium, which includes growth factors, cytokines, and supplements (no serum). [b]Values represent mean of three separate experiments.

(A)

Response marker	Fluorescent Probe	Excitation/ Emission	Response	Utility
Cell number/cell location	Hoechst 33342	355/465	Nuclear staining	Locating and counting of cells
Mitochondrial membrane potential	JC1	480/530-590	Shift of red to green fluorescence	Loss of MMP
Intracellular calcium	Fluo-4	480/510	Increased green fluorescence	Increased Intra-cellular calcium level
PI Uptake	Propidium Iodide	540/620	Increased PI uptake; red fluorescence	Compromised cell membrane integrity

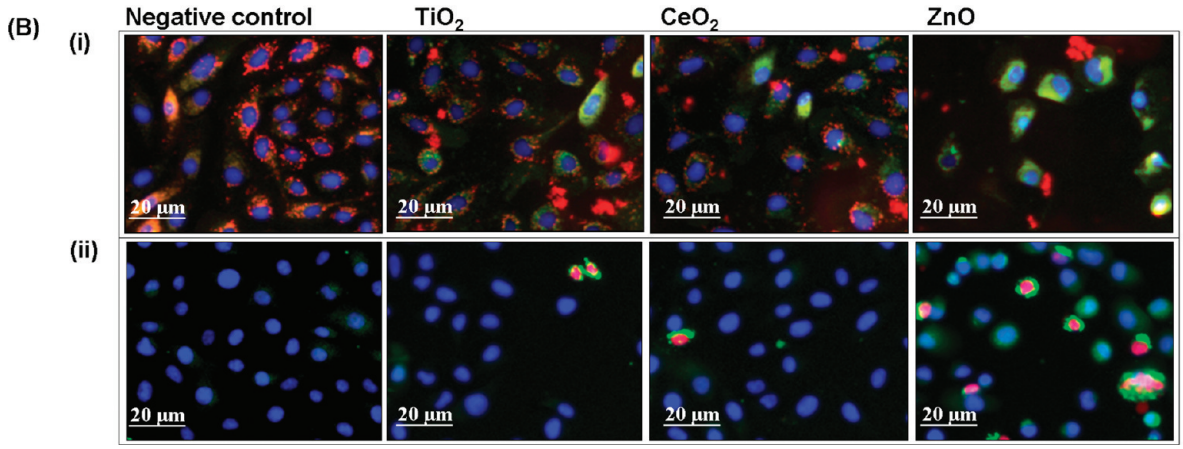

Figure 2. Fluorescence probes-properties and utilities. (A) Cytotoxicity markers and probes used in the study. (B) (i) BEAS-2B cells subjected to 3 h treatment with different NPs (50 μg/mL) were stained with Hoechst 33342 and JC1, simultaneously. The images of cells were captured by epifluorescence microscopy. Healthy cells (negative control) showed blue nuclei and red cytoplasm indicating healthy mitochondria. Mitochondria with decreased membrane potential cause the monomer formation of JC1 molecules, yielding green fluorescence. The percentage of cells with mitochondrial perturbation was highest in ZnO treatment group. TiO_2 treatment also resulted in a small population of cells with unhealthy mitochondria, while CeO_2 showed no sign of mitochondrial toxicity. (B) (ii) BEAS-2B cells subjected to 3 h treatment with different NPs (50 μg/mL) were stained with Hoechst 33342, Fluo-4, and propidium iodide (PI), simultaneously. Healthy cells showed blue nuclei while cells with membrane damage showed red nuclei. The increase in intracellular Ca^{2+} is shown as intense green cytoplasm. ZnO treated cells showed a distinct population of cells positive for both PI uptake and increased Fluo-4 intensity. TiO_2 and CeO_2 showed no significant increase in population of cells positive for PI and Fluo-4.

positive surface charges in water changed to negative, which is likely due to protein interaction with the metal oxide surfaces (Table 1). This effect is reflected in the zeta potential measurements shown in Table 1.

Development of Rapid Throughput Screening for Metal Oxide Nanoparticles by Epifluorescence Microscopy. While there are a number of different cellular injury responses to nanomaterials, we are interested in toxicological pathways that integrate multiple upstream injury mechanisms. In this regard, we have previously demonstrated that it is possible to stratify the *in vitro* hazard potential of engineered and ambient nanoparticles using a series of cellular assays that measure different tiers of oxidative stress (Supporting Information, Figure S1).[14,15,37] In fact, the oxidative stress paradigm has proven useful for comparing oxidant injury by engineered nanomaterials that exhibit properties such as electronically active surfaces (*e.g.*, semiconductor particles), absorption, or contamination with transition metals or redox cycling organic chemical impurities (*e.g.*, carbon nanotubes), photoactivation leading to the generation of electron−hole pairs (*e.g.*, TiO_2), or dissolution of the particle surface and shedding of toxic metal ions that induce ROS (*e.g.*, ZnO and chalcogenides).[1,14,15,37] Thus, to develop a rapid screening procedure for ZnO, CeO_2, and TiO_2 toxicity premised on oxidative stress injury, we initially experimented with fluorescent dye combinations to see if we can contemporaneously assess ROS production and oxidant injury. We observed, in accordance with our previous data,[15] that ZnO but not CeO_2 and TiO_2 under dark conditions could induce H_2O_2 and $O_2^{\bullet-}$ production in RAW 264.7 cells and BEAS-2B cells using dichlorofluorescein acetate (DCF) and MitoSox Red, respectively (Supporting Information, Figure S2). Unfortunately, it was not possible to combine these dyes with other fluorescent probes that assess cellular oxidant injury effects. However, we were able to find compatible dye combinations that could be combined in a multiparametric assay that assesses Tier 3 hierarchical oxidative stress responses (Figure 2A). These dyes include the DNA interactive agent, Hoechst 33342, JC1 (5,5′,6,6′-tetrachloro-1,1′,3,3′-tetraethylbenzimidazolylcarbocyanine iodide), Fluo-4, and propidium iodide (PI). The cell-permeable Hoechst

33342 binds to DNA, allowing us to count the number of nuclei and locate the cells on the culture dish. JC1 is a cationic dye that accumulates in the mitochondria of healthy cells. In this location, the dye exhibits red fluorescence but during a decrease of the mitochondrial membrane potential (MMP), the dye is released from this organelle allowing the monomer to accumulate in the cytosol where it fluoresces bright green. Therefore, the shift in fluorescence color from red to green is used to assess cells with compromised mitochondrial function. Propidium iodide (PI) is a red fluorescent dye that binds to DNA and is excluded from healthy cells by an intact plasma membrane. Damage of the plasma membrane in dying cells leads to the red fluorescence of the nucleus. Fluo-4 is a nonfluorescent cellular dye that is trapped inside living cells and fluoresces green when there is an increase in the cellular [Ca^{2+}], occurring during generation of oxygen radicals and release of toxic metal ions that damage subcellular organelles.[15] A visual example of the fluorescence changes captured by epifluorescence microscopy is shown in Figure 2B. In BEAS-2B cells treated with ZnO, the drop in MMP [panel (i)] is reflected as the appearance of green cytoplasmic fluorescence distinct from the granular and red fluorescence of mitochondria in untreated cells. The change in plasma membrane integrity and increase in intracellular calcium concentration, $[Ca^{2+}]_i$, manifest as increases in red and green fluorescence, respectively [panel (ii)].

With the dyes shown in Figure 2A, it was possible to develop an independent rapid screening procedure that performs dose- (0, 6.25, 12.5, 25, and 50 μg/mL) and time-dependent (0, 1, 2, 3, and 6 h) quantification of integrated toxic oxidative stress responses in RAW 264.7 and BEAS-2B cells (Figure 3 panels A and B, respectively). After correction for cell number and decrease in DNA content (Hoechst staining), ZnO nanoparticles could be seen to induce significant effects on intracellular Ca^{2+} flux, lowering of MMP, and loss of membrane integrity in both cell types. By contrast, CeO_2 and TiO_2 had little or no effect. The effect of ZnO on MMP, $[Ca^{2+}]_i$ increase and PI uptake in RAW 264.7 cells commenced at doses of 12.5−25 μg/mL and within 3−6 h of introducing the particles (Figure 3A). In contrast, all of the above responses were triggered in BEAS-2B cells in less than 2 h and by as little as 6 μg/mL ZnO (Figure 3B). Interestingly, TiO_2 generated small but significant decreases of MMP in both cell types without any significant effects on cell viability. CeO_2 did not exert any effect on any of the above response markers.

In summary, hazard profiling according to our 4-dye rapid throughput approach was nearly identical to the profiling obtained in our conventional assay procedures.[14,15] However, it should be noted that while conventional assay procedures that assess each cellular response individually in a dose- and time-dependent fashion in different cell lines takes 2−3 weeks to complete, the rapid screening procedure can be accomplished in a single sitting following prior plating of cells.

Use of Iron Doping to Synthesize ZnO Nanoparticles Exhibiting a Decreased Rate of Dissolution. We have previously demonstrated that the cytotoxic and pro-inflammatory effects of ZnO particles are related to particle dissolution intra- and extracellularly.[15] We hypothesized, therefore, that a change in nanoparticle dissolution characteristics through iron doping should lead to a decreased toxicity that could be assessed by our multiparametric procedure. Low resolution TEM (Figure 4A (a,b)), XRD (Figure 4B) and BET (Figure 4C) analyses showed a decrease in particle size with increasing iron concentration, a common trend when a dopant is incorporated into a host material during FSP synthesis.[32,38,39] SAED and power spectrum (Figure 4A (c−f)) combined with high resolution TEM (Figure 4A (g−h)) confirmed that iron loading up to 10.2 atomic percentage is possible without difference in the lattice spacings, phase segregation, and separate iron oxide particles. However, the crystal disorder in the doped particles increased with incremental Fe loading—likely due to oxygen vacancies that become the dominant source of structural disorder (Figure 4D). Pre- and postedge elemental mapping (Figure 5A) and EELS in STEM mode (Figure 5B) showed both Fe and Zn to be homogeneously distributed in the doped nanoparticles. An experimental inner-shell ionization Fe-L shell at 708 eV gave rise to an intense fine transition (Figure 5B) responsible for the overlapping of the electrons from the neighboring atoms involved in an interatomic bonding. The effect of iron doping on the dissolution of ZnO nanoparticles in aqueous solution were performed in electrolyte solution maintained at pH 7 ± 0.04 *via* pH stat control followed by aliquot extraction for dissolved zinc analysis (Figure 6A). After 10 days, Fe-doped nanoparticles appear to be less soluble than pure ZnO nanoparticles (Supporting Information, Figure S4). It is important to point out that lower zinc concentrations were observed for buffered *versus* pure aqueous solutions; we infer that true equilibrium was not reached after 10 days. Thus, the strong bonding of Fe in the host lattice of ZnO is responsible for the significant reduction of ZnO nanoparticle dissolution. The presence of iron in the ZnO lattice affected the nanoparticle surface properties when suspended in water and cell culture media (Figure 6B). This is reflected by a decrease in zeta potential in water with incremental Fe doping levels (Figure 6B). However, in the presence of protein containing cell culture media, all the particles had approximately the same negative charge. In spite of the decrease in primary particle size with incremental dopant level (Figure 4C), the average particle size in aqueous media was slightly bigger but still in the nm range (Figure 6B).

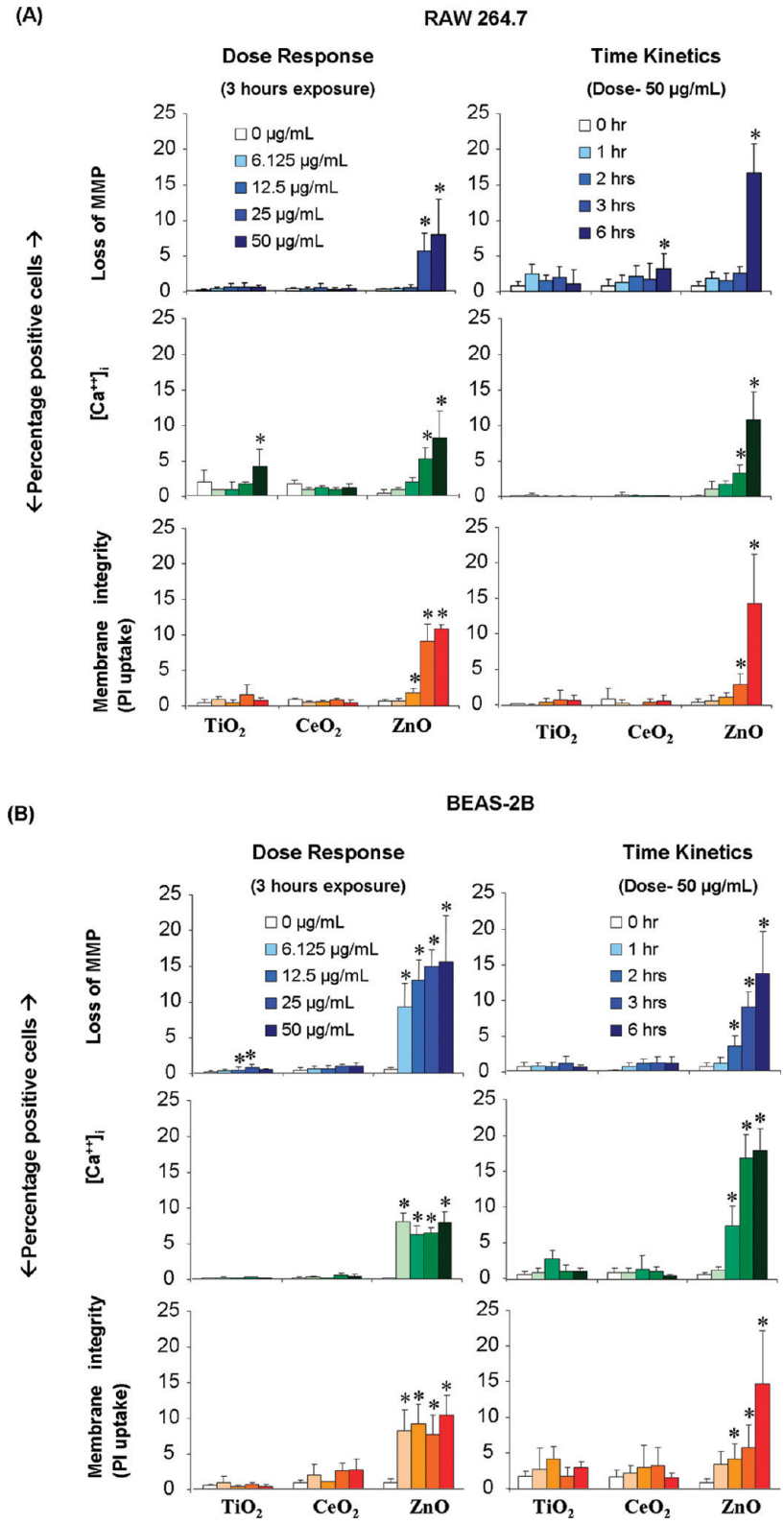

Figure 3. Multiparametric assay to compare the cytotoxicity of metal oxide NPs in RAW 264.7 and BEAS-2B cells. Cell plating, particle dispersion, and addition to the tissue culture plates, cell staining and epifluorescence microscopy were performed as described in materials and methods. After exposure to NPs suspended in respective growth medium at 6.125−50 μg/mL for 3 h (dose response) or exposed to 0.1−6 h at 50 μg/mL concentration (time kinetics), RAW 264.7 (A) and BEAS-2B cells (B) were stained for 30 min with the dye cocktails that contemporaneously assess mitochondrial membrane potential (JC1, 1 μM), intracellular calcium flux (Fluo4, 5 μM) and membrane damage (PI, 5 μM). The percentage of cells positive for the given cytotoxic response was scored from fluorescence image cells using MetaXpress software. The error bar indicates standard deviation from mean value obtained from nine replicates; *$p < 0.05$, comparison is with 0 dose or duration of exposure. Number of repeat experiments = 3.

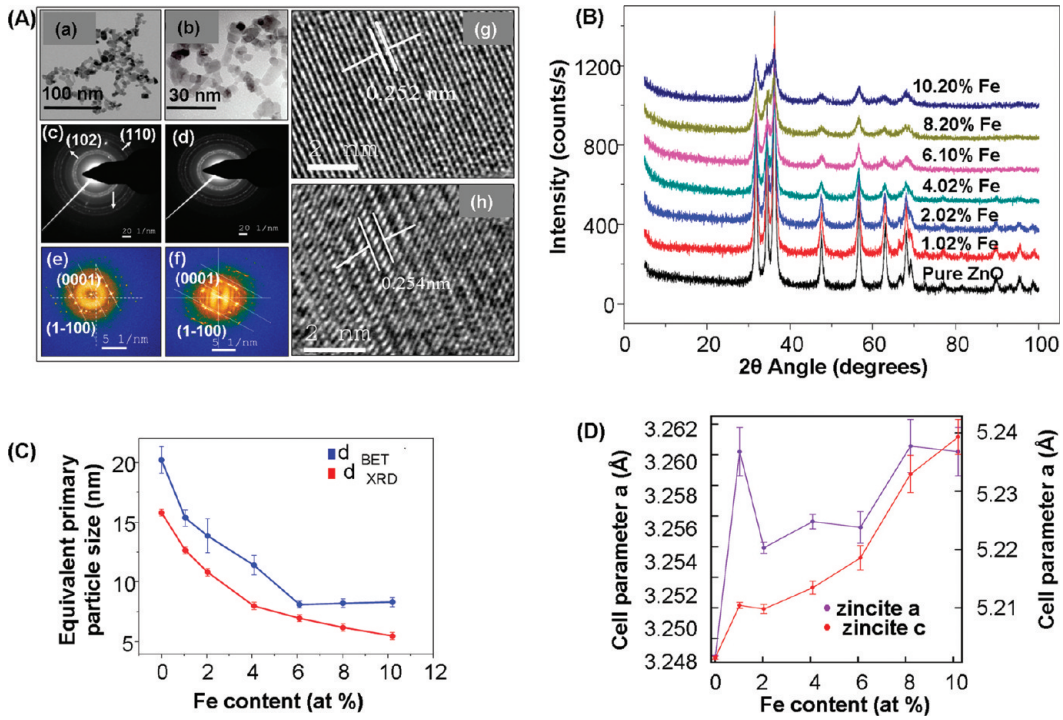

Figure 4. Physicochemical characterization of iron-doped ZnO NPs. (A) Low resolution TEM of pure ZnO (a) and 10.2% Fe-doped ZnO (b). SAED patterns of pure ZnO (c) and 10.2% Fe-doped ZnO (d). Power spectrum of single crystalline pure (e) and 10.2% Fe-doped ZnO nanoparticles (f) showing no changes in the crystal structures of the NPs. High resolution TEM images of the pure ZnO (g) and 10.2% Fe-doped ZnO NPs (h). (B) XRD patterns of pure and Fe-doped ZnO NPs. (C) Equivalent primary particle size obtained using XRD and BET surface area measurements. Error bar indicates standard deviation from mean value. (D) Variation in the lattice parameters with increasing Fe loading. The trend in the change of the parameters are the same for $a = b$ and c with increasing Fe content. Error bar indicates standard deviation from mean value.

Demonstration That Iron Doping and Change in ZnO Dissolution Leads to Reduced Cytotoxicity as Demonstrated in the Multiparametric Assay. To test the hypothesis that reduced dissolution can improve nanomaterial safety, the cytotoxic effects of the panel of doped and undoped ZnO nanoparticles were evaluated using our rapid screening approach. In RAW 264.7 cells the mean % of cells positive for PI staining or cells exhibiting increased $[Ca^{2+}]_i$

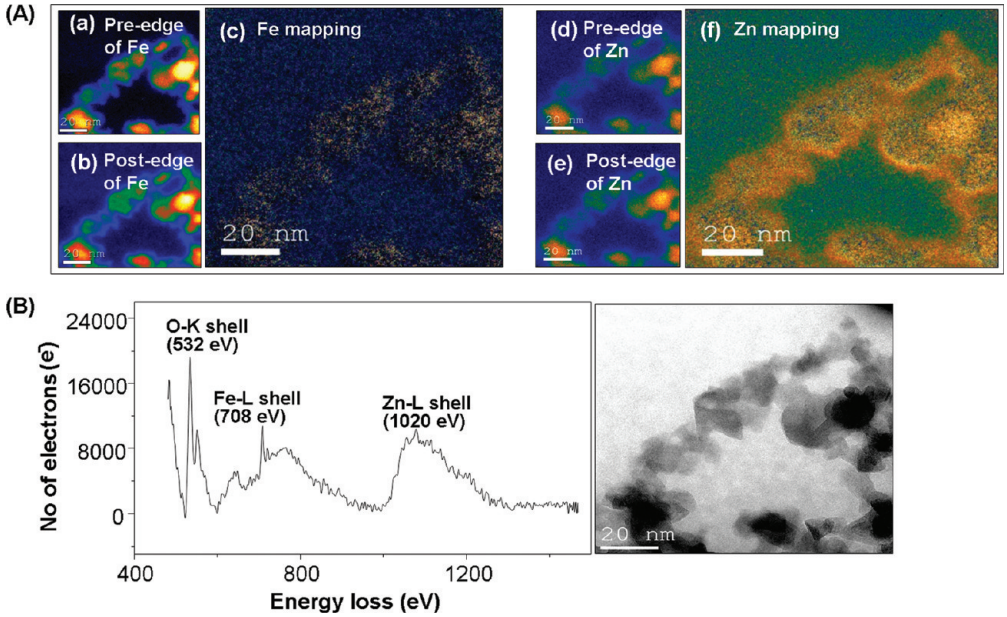

Figure 5. Distribution of Fe in crystal structure of ZnO NPs. (A) The elemental mapping (EFTEM) of 10% Fe-doped ZnO NP: (a,b), pre-edge and postedge of Fe mapping, (c) Fe mapping in the wide spot of the NP distribution, (d,e) pre-edge and postedge of Zn, (f) Zn mapping in the same wide spot of the NP distribution. (B) EELS spectrum of 10.2% Fe-doped ZnO NPs. The energy loss value of 708 eV from the L shell (1s2 2p6) shows clear indication of the homogeneous Fe distribution in the ZnO matrix.

(A)

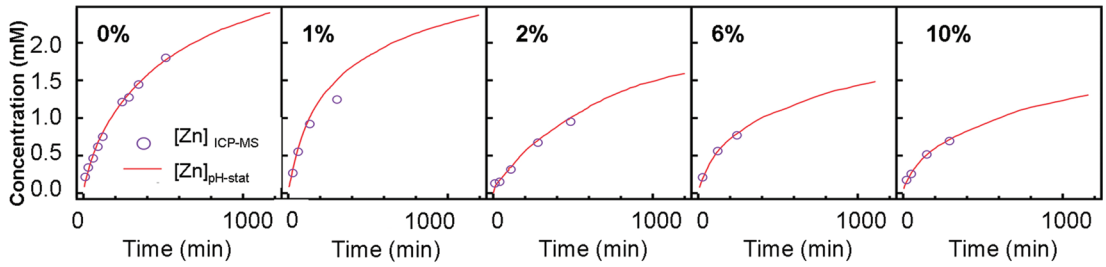

(B)

NPs	Size (nm)			Zeta potential (mV)		
	Water	CDMEM	BEGM+BSA (2mg/mL)	Water	CDMEM	BEGM+BSA (2mg/mL)
ZnO	130.5	24.23	45.17	13.2	-10.3	-9.92
ZnO+1.02% Fe	658.9	35.71	71.63	1.11	-10.3	-10.1
ZnO+2.04% Fe	653	51.15	81.83	2.44	-10	-12.6
ZnO+4.09% Fe	835.3	77.06	107	-1.12	-7.91	-11.4
ZnO+6.1%Fe	1582	100.47	122.6	-4.04	-10.6	-7.74
ZnO+8.2% Fe	1754	100.77	132.8	-11	-9.44	-10.5
ZnO+10.2%Fe	1780	104.1	141.5	-13.9	-8.92	-7.97
Fe_3O_4	143.7	367.3	382.4	-24.5	-10.2	-11.1

Figure 6. Dissolution kinetics and physicochemical characteristics of iron-doped ZnO NPs in aqueous media. (A) The rate of zinc release into aqueous solution at pH 7 by the dissolution of pure and Fe-doped ZnO nanoparticles. ZnO dissolution and Zn^{2+} release was studied by adding 6.7−6.9 mg of material to 25 mL of a 0.1 M sodium perchlorate solution at pH 7. The kinetics of Zn^{2+} was followed by measuring the amount of nitric acid added to maintain the pH and by periodic sampling to assay for Zn content using ICP-MS. (B) The effect of iron doping on ZnO size and zeta potential. Please notice that the increase in mean particle size with incremental atomic percentages of Fe is due to particle agglomeration, which tended to be larger in the low protein (BEGM) compared to the higher protein (CDMEM) medium.

flux could be seen to decrease ~50% at the lowest Fe doping level (1.02%); this trend continued with increasing dopant levels and is statistically significant for doping levels and for every response being measured (Figure 7A). Similarly, Fe doping slowed the loss of MMP, PI uptake, and $[Ca^{2+}]_i$ increase in BEAS-2B cells with increased atomic percentage of Fe (Figure 7B). While all the responses returned to baseline at the highest dop-

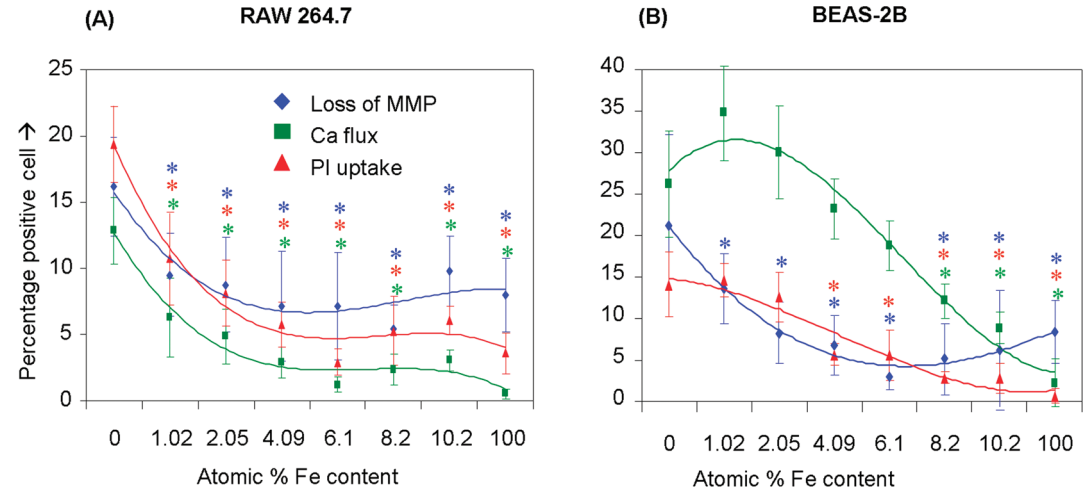

Figure 7. Multiparametric assay showing the effect of iron doping on the cytotoxicity of nano ZnO. After exposure to NPs suspended in respective growth medium at 6.125−50 μg/mL for 3 h, cells were stained with our dye cocktail (refer to Figure 3 legend). The percentage of cells positive for a given response parameter was scored using MetaXpress software. (A) RAW 264.7 cells subjected to NP treatment showed a significant decrease in cytotoxic effects such as drop in MMP, increase in intracellular calcium level, and cell membrane damage as the atomic percentage of Fe in ZnO increases. (B) BEAS-2B cells subjected to nanoparticle treatment showed a significant decrease in cytotoxic effects such as rise in $[Ca^{2+}]_i$ and cell membrane damage as the atomic percentage of Fe in ZnO increases. (Error bar indicates standard deviation from mean value obtained from nine replicates; *$p < 0.05$, comparison is with no doping).

ing level, the rates of decline were not as steep as RAW 264.7 cells, especially for the decline in MMP. These response differences could relate to differences in the routes of cellular nanoparticle uptake, including differences in the rate of dissolution of ZnO in the lysosomal and caveolar compartments of RAW 264.7 and BEAS-2B cells, respectively.[15]

DISCUSSION

In this communication, we demonstrate that it is possible to use a key pathway of nanomaterial toxicity to develop a rapid throughput assay procedure to assess the cytotoxic potential of three metal oxide nanoparticles, previously ranked for their toxic potential by conventional oxidative stress assays. Among the three metal oxide nanoparticles evaluated, ZnO was comparatively more toxic in our multiparametric assay that assesses plasma membrane damage, $[Ca^{2+}]_i$ flux, and mitochondrial depolarization. Because we have previously demonstrated in the conventional assays that ZnO nanoparticles are capable of inducing tier 2 and 3 oxidative stress responses through Zn^{2+} release, we used iron doping to test the hypothesis that decreased dissolution might decrease the cytotoxic potential of ZnO nanoparticles. We demonstrate through detailed physicochemical characterization that iron doping changes the ZnO nanoparticle matrix. These data demonstrate that it is possible to perform hazard ranking of chemically related nanomaterials by using an integrated biological injury pathway. We also demonstrate that if the nanomaterial property associated with the injury response is known, it is possible to use our biological screening assay to show that a composition change could affect material safety.

This is the first description of a multiparametric assay that utilizes toxic oxidative stress to perform rapid screening of nanoparticle toxicity. To use a fluorescence-based approach, it was necessary to obtain proper nanoparticle dispersal to avoid the artifacts that can be introduced by sedimenting agglomerates. This was achieved by using a protein-based nanoparticle dispersion strategy to stabilize the particles in deionized water prior to the introduction into protein containing tissue culture media. BSA and possibly other serum proteins are known to transiently adsorb to metal oxide surfaces,[36] which could explain their stabilizing effects through steric hindrance and electrostatic effects (Table 1). A second issue that was addressed was the compatibility of fluorescence dyes included in our multiparametric assay. The dye combinations that we settled on after serial experimentation were stable over the duration of the experiment and allowed contemporaneous assessment of cellular responses. We also carried out pilot studies where the dyes incubated with nanoparticles in the absence of cells to exclude the possibility of false positive results due to dye interactions with the particle surfaces. Further, the reliability of the cellular responses included in our screen was confirmed by traditional methodology (*e.g.*, flow cytometry, ELISA, or fluorometry) to assess membrane permeability changes, ATP content, or metabolic activity. Apart from these precautions, we standardized the optimal number of cells ($\sim 1 \times 10^4$ cells per well of 384 well plate), optimal dye concentrations, and incubation times with the dyes. A desired response characteristic that we could not introduce to the multiparametric assay was cellular ROS production; this was due to incompatibility of the DCF and MitoSOX Red wavelengths with our selected dye combination (Figure 2A). However, we did demonstrate that inclusion of these dyes in a parallel epifluorescence procedure could demonstrate increased H_2O_2 and superoxide generation by ZnO (Supporting Information, Figure S2), which is in accordance with the higher cytotoxic potential of these particles (Figure 3).

There are numerous biological and molecular events that prestage or accompany the induction of cell death in response to engineered nanomaterials (Figure 8). These include immediate biological injury requiring direct physical presence of hazardous nanomaterials as well as more distal injury responses that originate due to afferent injury. Cytotoxicity is an example of a downstream injury response to more immediate particle effects involving ROS production such as photoactivation (*e.g.*, electron−hole pair formation during UV activation of TiO_2), surface shedding of toxic metal ions that trigger cellular ROS generation (*e.g.*, interference in mitochondrial electron transduction by cationic nanoparticles or dissolved Zn^{2+}), electronically active surfaces (*e.g.*, semiconductors), and presence of redox cycling chemical compounds (*e.g.*, transition metal impurities in carbon nanotubes).[1,40] While our assay captures the events at the highest tier of oxidative stress (Tier 3), our attempts to develop a multiparametric assay that also includes Tiers 1 and 2 were unsuccessful due to the labor intensiveness of such a procedure. We intend, however, to include the lower tier oxidative stress responses in future efforts because we believe that those responses do have clinical toxicological relevance. For instance, the *in vitro* oxidative stress profiling of ZnO nanoparticles have shown features that are analogous to the disease features of metal fume fever, an acute inflammatory condition of the lung in welders who are exposed to aerosolized metal oxide nanoparticles.[41,42] For instance, the expression of a tier 2-like response in macrophages and epithelial cells, characterized by interleukin 8 (IL-8) and TNF-α production, is reflective of similar cytokine production in the lungs and bronchoalveolar lavage fluid of exposed workers.[15] In addition, metal fume fever is characterized by an adaptive response where prior exposure to welding fumes can avert metal fume fever upon re-exposure.[43] This is reminiscent of a tier 1-like adaptive response.

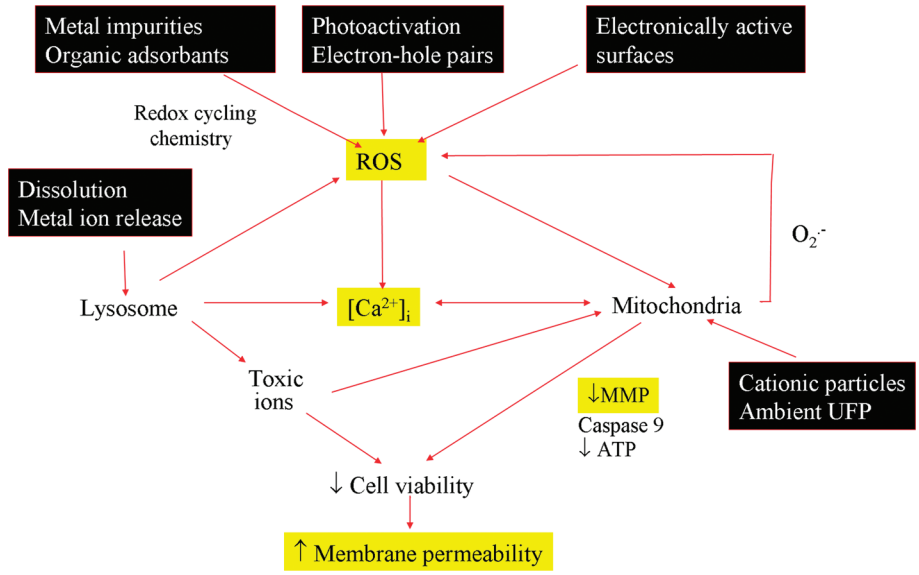

Figure 8. Schematic to illustrate the interrelatedness of cellular responses in our multiparametric assay and the linkage to nanoparticle-induced ROS production. Nanomaterials induce ROS production as a direct consequence of specific material properties or as a consequence of triggering cellular injury responses leading to oxidant radical generation. ROS production could trigger a range of oxidative stress effects as outlined in the hierarchical oxidative stress model shown in Supporting Information, Figure S1. The induction of cellular toxicity at the highest level of oxidative stress involves a number of interrelated cellular responses that include intracellular Ca^{2+} release and mitochondrial perturbation leading to cell death with accompanying changes in cell membrane integrity and nuclear PI uptake. We have previously demonstrated that ZnO nanoparticles engage this toxic oxidative stress pathway through an event sequence that includes particle dissolution, shedding of Zn^{2+}, $[Ca^{2+}]_i$ flux, superoxide generation, and mitochondrial perturbation.[15] The schematic outlines the particle characteristics that could culminate in cytotoxicity.

Our multiparametric assay assesses the change in membrane permeability that develops in dying cells.[44] In addition, our assay measures $[Ca^{2+}]_i$ flux and mitochondrial depolarization that are functionally linked insofar as oxidative stress can trigger Ca^{2+} influx from the extracellular medium as well as from sequestered intracellular stores, such as the endoplasmic reticulum.[45] Oxidative stress also inhibits Ca^{2+} transport from cytoplasm by inhibiting ATPase pumps such as sarco/endoplasmic reticulum Ca^{2+}-ATPase (SERCA).[46] The rise in $[Ca^{2+}]_i$ simulates Ca^{2+} uptake into the mitochondria *via* uniporters. If this buffering action exceeds the threshold for mitochondrial Ca^{2+} sequestration, this could trigger large-scale opening of the permeability transition pore (PT pore), mitochondrial depolarization, and the release of pro-apoptotic factors.[47] This response is further enhanced by oxidative cross-linking of vicinal thiol groups in the PT pore.[48] Thus, by combining membrane permeability with $[Ca^{2+}]_i$ flux and mitochondrial depolarization, we have established a multiparametric assay that goes beyond live/dead scoring. Figure 8 summarizes this relationship. Please notice that $[Ca^{2+}]_i$ flux and mitochondrial depolarization can also be achieved by nonoxidative injury pathways. This illustrates the importance of evaluating ROS generation to establish a relationship to oxidative stress. While we are currently unable to incorporate ROS production into the assay, it is possible that this could be achievable with future advances in cell imaging.

While there was good agreement in the hazard ranking of the metal oxides in the rapid throughput and conventional assay procedures,[15] the former assay is accomplishable in 1 day *versus* the 2−3 weeks to complete the conventional assays. There is also good agreement between the results in RAW 264.7 and BEAS-2B cells, which were chosen because of differences in nanoparticle endocytic uptake routes.[15] Thus, while the ZnO particles were mostly localized in a LAMP-1 positive compartment in RAW 264.7, the predominant uptake route in BEAS-2B cells are caveolae.[15] Differences in the acidification and Zn^{2+} release in these compartments may determine the cascade of events leading to cytotoxicity (Figure S3).[15] While the exact molecular details of this complicated train of events requires further study, our multiparametric assay demonstrates that it is possible to integrate key responses into a functional assay. In addition to drawing on these integrated responses, we foresee that a series of cellular response characteristics can be combined in cytotoxicity screening. Recently, a multidimensional assay was used as a rapid throughput procedure to compare the decrease in cell viability in response to a panel of paramagnetic iron oxide nanoparticles used for imaging purposes.[12] These authors measured cytotoxic events such as ATP content, reducing equivalents, caspase-mediated apoptosis and MMP in different cell lines. Their analysis enabled them to identify nanomaterials with similar biologic activities.[12] Further, the predictive power of multiparametric *in vitro* assays was demonstrated under *in vivo* conditions.[12]

Since the critical steps in our multiparametric assay (*e.g.*, cell seeding, liquid handling, imaging, image

analysis, *etc.*) are automated, it is quite feasible that this test protocol can be further developed for high content or high throughput screening for a combinatorial library such as demonstrated for the doped ZnO series (Figure 7). We have just begun to expand the automated assay to assess large batches of nanomaterials not previously subjected to comparative screening and are currently able to analyze 5120 different variables in 5 days. This approach can speed up the knowledge generation and safety profiling of large batches of new nanomaterials that are entering the marketplace.[40] In addition, the use of high throughput screening could lead to the discovery of unknown toxicological pathways. If, for instance, our procedure should reveal a cytotoxic material that does not generate ROS, this could prompt us to look at additional injury mechanisms such as surface membrane or DNA damage. It is also possible to envisage the emergence of a number of multiparametric assays that assess nonoxidant injury mechanisms such as the protein unfolding response,[49] triggering of immune "danger signals", activation of signaling cascades,[18] mitochondrial permeability transition pore opening, and apoptosis.[3,50]

For the *in vitro* screening assay to be a truly predictive toxicological tool, the assay results has to be linked to *in vivo* toxicological analysis.[40] Thus, the *in vitro* screening assay only constitutes one step in nanomaterial safety assessment. We have therefore engaged in a series of experiments in the University of California Center for the Environmental Implications of Nanotechnology (UCCEIN) to determine what effects the three metal oxides may have on a trophic series of life forms in freshwater, seawater, and terrestrial mesocosms.[51] The data that are emerging and currently being compiled for publication indicate that ZnO nanoparticles are indeed more toxic than TiO_2 and CeO_2 in environmental life forms such as bacteria, phytoplankton, plants, crustaceans, and zebra fish. This is in agreement with a recent nanoecotoxicological review of the effects of metal oxide nanoparticles, which documents that nano ZnO should be regarded as "extremely toxic" compared to the "harmful" labeling of nano TiO_2.[52] Moreover, it has also been clearly established that ZnO nanoparticle toxicity in the environment is dependent on solubilization and yields median $L(E)C_{50}$ values of 0.06 μg/mL for algae, 1.9 μg/mL for fish, 5.4 μg/mL for ciliates, 20 μg/mL for bacteria, and 121.2 μg/mL for yeasts.[55] At present, data on real environmental concentrations of ZnO nanoparticles are scarce. However, a number of physicochemical and biotic factors contribute toward the magnification of nanoparticle concentration in environment,[52] necessitating the inclusion of a range of concentrations in toxicological studies. For metal fume fever an 8-h threshold limit value of 5 mg/m^3 and 15-min short-term exposure limit of 10 mg/m^3 have been established to prevent adverse health effects by inhaling ZnO fumes; the exact intrapulmonary dose at sites of ZnO nanoparticle deposition and dissolution is unknown. However, we have previously demonstrated in the dose calculation for ambient fine particle that impact so-called hotspots of deposition in the lung that it is possible to achieve surface doses comparable to that in tissue culture dishes.[53]

On the basis of the importance of nanoparticle dissolution to ZnO toxicity, we hypothesized that lowering the rate of dissolution could decrease cytotoxicity. Since, mixed zinc−iron oxides are significantly more resistant to proton-assisted dissolution than pure zincite,[54] we investigated the impact of iron doping on ZnO dissolution and cytotoxicity. As postulated, iron doping enhanced the aqueous stability of ZnO through strengthening of iron *versus* zinc binding to oxygen.[41] Consistent with this mechanism, we observed reduced dissolution after 10 days in buffered solution for iron-doped nanoparticles, although true equilibrium may not have been attained (Supporting Information, Figure S4). While the oxidation state of iron atoms doped in ZnO depends on the synthesis method and handling,[55] iron is typically found to be present as high spin Fe^{2+} ions substituted for Zn^{2+} at lattice sites.[55,56] Consideration of the crystal field splitting of the Fe 3d states (Supporting Information, Figure S5) implies Fe^{2+} to be more strongly bound than Zn^{2+} despite lack of change in the Madelung contribution to the lattice energy. Iron atoms may also introduce a kinetic constraint for zinc release into solution,[54] particularly if they preferentially segregate to surface sites as suggested by the zeta-potential measurements. In addition, iron is an environmental friendly element that is abundantly found in the biological systems, making it an ideal candidate for designing safer nanomaterials.[57]

Consistent with the material properties of the doped particles, the cytotoxicity evaluation showed decreased ZnO cytotoxicity with incremental atomic percentages of iron (Figure 7). While most of the toxicity parameters returned to normal at 4% Fe doping in RAW 264.7 cells, the decline was more gradual in BEAS-2B cells. These differences could be due to differences in the intracellular processing and endosomal acidification mechanism as discussed earlier.[15] While it is possible that the change in doped particle size may have contributed to the biological effects, we did not observe a change in particle uptake when using TEM to compare high and low Fe-doped particles (not shown). However, further work is required and we will use techniques such as soft X-ray scanning transmission microscopy, micro-X-ray fluorescence, atomic force microscopy (AFM), and environmental SEM to further dissected intracellular fate and dissociation of nano ZnO.

It is important to emphasize that cytotoxicity screening as a lone-standing exercise has several limitations and that the true toxicological significance of a cellular injury response can only be determined if it is associated with adverse biological effects in intact organisms

and animals.[40] Although, many studies point toward the possibility of extrapolating *in vitro* toxicity to *in vivo* toxicity,[15,58] one of the major concerns using *in vitro* assessment is that it can never represent all the events that shape *in vivo* toxicity. However, *in vitro* studies are excellent tools for studying cellular injury pathways and as a data gathering tool for prioritizing *in vivo* studies.

CONCLUSION

We demonstrate that our rapid multiparametric screening procedure is capable of assessing changes in cell viability through an integrated toxicological paradigm. ZnO was comparatively more toxic than TiO_2 and CeO_2 nanoparticles based on the principle of particle dissolution and shedding of toxic Zn^{2+}. This toxicity could be reduced by iron doping which leads to a stabilization of material crystal structure. In ZnO containing sunscreens, for instance, subtle changes in crystal structure may not compromise their protection against sunlight although it may affect the electrical and magnetic properties of this material. Overall, our study demonstrates the utility of integrated cytotoxicity screening assays to assess nanomaterial hazard as well as how to improve material safety through rational modification of toxicological properties.

MATERIALS AND METHODS

FSP Synthesize of Metal Oxide Nanoparticles. For FSP, the metallorganic based precursors, titanium isopropoxide (Aldrich), cerium(III) 2-ethylhexanoate (49% in 2-ethylhexanoic acid) and zinc napthenate (8% of Zn by metal, Strem) were used for the synthesis of the respective metal oxide nanoparticles. A 50 mL portion of 0.5 M zinc napthenate was separately mixed with 0.6−6.0 mL of 0.5 M iron napthenate to make 1−10% of Fe doping in ZnO. All the precursors were dissolved in an organic solvent (xylene, 99.95%, Strem) to keep the metal to 0.5 M except for the cerium precursor that was used at 0.27 M. Each liquid precursor was delivered to the nozzle tip by a syringe pump at a flow rate of 5 mL/min by atomizing the precursor solution with dispersant O_2 at a flow rate of 5 mL/min and maintaining a pressure drop of 1.5 bar at the nozzle tip. Combustion of the dispersed droplets is initiated by the codelivery of CH_4 and O_2 (1.5 L/min, 3.2 L/min) to form a flame.[59]

Nanoparticle Dispersion in Cell Culture Media. Nanoparticle stock solutions (5 mg/mL) were prepared by dispersing the nanoparticle powder in deionized water by probe sonication (3 W). To ensure proper dispersion of nanoparticles, the stock solution was sonicated before removing aliquots to prepare working solutions. To coat the surface of nanoparticles with bovine serum albumin (BSA), the aliquoted nanoparticle suspension (~10 μL) was mixed with an equal volume of 4% BSA (Fraction-V; Gemini Bioproducts, USA) and equilibrated for 1 h at room temperature. Cell culture media (1 mL) were added to the BSA-coated nanoparticle suspensions. The particle suspensions in BEGM were further stabilized by the addition of BSA at a final concentration of 2 mg/mL. The nanoparticle suspensions were sonicated (3 W) for 15 s prior to the addition to tissue culture plates.

Aggregate Size Distribution and Zeta Potential Measurement. Aggregate size distribution (PSD) was assessed in a ZetaSizer Nano (Malvern Instruments, Westborough, MA). This instrument measures DLS (173°) of nanoparticles in the range of 100−6000 nm by backscattering. The same instrument was used to measure the electrophoretic mobility of nanoparticle suspensions. Electrophoretic mobility is used as an approximation of particle surface charge and is transformed into zeta-potential using the Helmholtz−Smoluchowski equation. Particle size distribution and electrophoretic mobility were performed in complete cell culture media at pH 7.4.

Brunauer−Emmett−Teller (BET) and X-ray Diffraction (XRD) Analysis of Nanoparticles. N_2 adsorption−desorption measurements were carried out at 77 K using a Quantachrome NOVA 4000e Autosorb gas sorption system. The BET method was used to determine the specific surface areas of the samples. The powders were placed in a test cell and allowed to degas for 2 h at 200 °C in flowing nitrogen. Data were obtained by introducing or removing a known quantity of adsorbing gas in or out of a sample cell containing the solid adsorbent maintained at a constant liquid nitrogen temperature. The specific surface area of ZnO, CeO_2, and TiO_2 were found to be 52.11 (±0.13), 164.03 (±2. 22), 144.91(±3.16) m^2/g corresponding to particle sizes of 20.2, 5.01, and 9.71 nm, respectively. XRD was collected in a reflection mode on the PW 3040/60 X'Pert PRO diffractometer equipped with X'Celerator linear detector using a Cu Kα (λ = 0.154 nm) radiation and step size of 0.01°.

Transmission Electron Microscopic Analysis of Nanoparticles. The FSP-generated metal oxide nanoparticles were sonicated (water bath) in ethanol for 3 h before TEM analysis. The microscopic imaging of the specimens were investigated with a FEI Titan 80/300 microscope equipped with a Cs corrector for the objective lens, a Fischione high angle annular dark field detector (HAADF), GATAN postcolumn imaging filter, and a cold field emission gun operated at 300 kV as an acceleration voltage. To obtain EELS spectrum, Gatan parallel EELS spectrometer was operated at 0.2 eV per channel as an energy dispersive detector. Kevex energy dispersive X-ray spectrometer was used at 10 eV per channel for EELS spectra, SAED patterns, and EDX. Spectra were taken at each sampling point in order to identify the homogeneity of the samples. EFTEM images of pre- and postedges of elemental mappings were obtained from the data by energy calibration and background subtraction. Zero loss and low loss spectra were also taken at each sampling point for energy calibration and for sample thickness. Calibration was made by using the energy of the zero loss, low loss, or core loss at the lower energy.

Cell Culture and Coincubation with Nanoparticles. All cell cultures were maintained in 25 cm^2 cell culture flasks, in which the cells were passaged at 70−80% confluency every 2−4 days depending on the cell type. Recently thawed RAW 264.7 cells (ATCC no. TIB71) were cultured in Dulbecco's modified eagle medium (DMEM) (In Vitrogen, Carlsbad, USA) containing 10% FBS, 100 U/mL penicillin, 100 μg/mL streptomycin, and 2 mM L-glutamine (complete medium).[15] These cells were plated at 5000 cells per well into 384 well plates (CellBound, Corning Inc., MA). Cells were cultured overnight at 37 °C in a 5% CO_2 incubator before nanoparticle treatment. BEAS-2B (ATCC no. CRL-9609) cells were cultured in BEGM (Lonza, San Diego, CA) in type-I rat tail collagen-coated flasks. Trypsinized cells were washed and plated at 5000 cells per well (in 50 μL) into 384 well plates. RAW 264.7 cells were cultured overnight at 37 °C in a 5% CO_2 incubator while BEAS-2B cells were cultured for 2 days before nanoparticle treatment. Nanoparticles prior coated with BSA and then dispersed in CDMEM or BEGM added with 2 mg/mL BSA were used to treat RAW 264.7 and BEAS-2B cells, respectively. Nanoparticle exposures were carried out at concentrations of 6.25, 12.5, 25, and 50 μg/mL for 3 h or were exposed to 50 μg/mL nanoparticles for 1, 2, 3, and 6 h.

Cellular Staining with Fluorescent Probes and High Content Epifluoresence Microscopy. Two cocktails of fluorescent probe mixtures were prepared by mixing wavelength-compatible fluorescent probes in DMEM media devoid of phenol red. The first cocktail contained Hoechst 33342 (1 μM) and JC1 (1 μM) while the second cocktail contained Hoechst 33342 (1 μM), Fluo-4 (5 μM), and propidium iodide (5 μM). The utility of these dyes, their excitation−emission wavelengths, and cellular responses are summarized in Figure 2A. Cells in each well of the multiwell

plates were incubated with 50 μL of dye mixture for 30 min under standard cell culture conditions in the dark. Unincorporated dyes were removed by washing, following which tissue culture wells were replenished with phenol red-free DMEM or BEGM. Plates were acquired on an Image-Xpress^{micro} (Molecular Devices, Sunnyvale, CA) equipped with laser autofocus. Images were processed using MetaXpress (Molecular Devices, Sunnyvale, CA) under a 10× magnification. DAPI, FITC, and TRITC filter/dichroic combinations were used to image Hoechst 33342 (blue), Fluo-4 (green), and PI (red), respectively. The total number of nuclei was counted using the following thresholds: In the Hoechst/DAPI channel the approximate minimum width was 3 μm (about 3 pixels) and the approximate maximum width was 10 μm (about 7 pixels). The intensity above background level was 100 gray levels. For the FITC and TRITC channels the approximate minimum width was 5 μm (about 6 pixels) and the approximate maximum width is 30 μm (about 22 pixels). The intensity above background is 250 and 500 gray levels, respectively. The percentage of cells positive for a given cellular response was calculated on the basis of the total number of cells (Hoechst 33342 positive cells) and total number of cells having fluorescence intensity above the defined threshold intensity for that parameter. The raw data were exported to an Excel file for comparison and statistical analysis.

ZnO Nanoparticle Dissolution Studies. The effect of iron doping on the rate of ZnO dissolution and Zn^{2+} release was studied by adding 6.7−6.9 mg of material to 25 mL of a 0.1 M sodium perchlorate solution at pH 7 and 22 °C. Following an initial pH drop, the pH rebounded as expected for the reaction

$$ZnO_s + 2H^+ \rightarrow Zn^{2+}_{aq} + H_2O \quad (1)$$

Solution pH was maintained at pH 7.0 ± 0.4 by the addition of nitric acid controlled by the pH stat function of a Mettler-Toledo T70 autotitrator. The reaction was followed by recording the addition of acid with time and by periodic sampling of 100 μL aliquots for total zinc analysis following dilution with 1 mL of electrolyte solution and centrifugation for 5 min at 20000*g* to remove nondissolved suspended nanoparticles. A 500 μL portion of supernatant was acidified with 500 μL of 7% ultra high purity nitric acid, and the zinc ion concentration, [Zn], was measured with inductively coupled plasma mass spectrometry (ICP-MS) using Perkin-Elmer SCIEX Elan DRCII. There was close agreement between the measured [Zn] and the predicted concentrations based on the rate of acid addition assuming eq 1, indicating this to be the dominant process, with no significant formation of solid or aqueous phase protonated species, as expected for pH 7. We used the phreeqc code to estimate the equilibrium concentration of Zn (aq) in 0.1 M $NaClO_4$ at pH 7 due to the dissolution of bulk zincite at 25 °C. [Zn] eq ≈ 4.4 mM, indicating that equilibrium was not reached during the dissolution studies.[60]

The effect of iron doping on the long-term dissolved zinc concentration was studied by equilibrating 1 mg of each nanomaterial with 1 mL of a 0.1 M solution of 1,4-piperazinediethanesulfonic acid (PIPES) buffer at pH 7 for 10 days. The PIPES buffer exhibits weak affinity for divalent metal ions and thus was not anticipated to affect the zinc oxide solubility product through complexation with aqueous species. The samples were centrifuged for 1 h with temperature control, and 100 μL of supernatant was removed for ICP−MS analysis of total zinc.

Acknowledgment. This work is supported by the National Science Foundation and the Environmental Protection Agency under Cooperative Agreement Number EF 0830117. Any opinions, findings, conclusions, or recommendations expressed herein are those of the author(s) and do not necessarily reflect the views of the National Science Foundation or the Environmental Protection Agency. This work has not been subjected to an EPA peer and policy review. Key support was provided by the UC Lead Campus for Nanotoxicology Training and Research, funded by UC TSR&TP, US Public Health Service Grants (U19 AI070453, RO1 ES016746, and RC2 ES018766) and the US EPA STAR award (RD-83241301) to the Southern California Particle Center. B.G. acknowledges funding from DOE BES DE-AC02-05CH11231 and thanks Joern Larsen for the ICP−MS analysis.

Supporting Information Available: Hierarchical oxidative stress paradigm, assessment of ROS production by metal oxide NPs, mechanism of ZnO NP mediated cytotoxicity, dissolution of Zn^{2+} from iron-doped ZnO NPs, proposed model for reducing Zn^{2+} dissolution from ZnO NPs. This material is available free of charge *via* the Internet at http://pubs.acs.org.

REFERENCES AND NOTES

1. Nel, A.; Xia, T.; Mädler, L.; Li, N. Toxic Potential of Materials at the Nanolevel. *Science* **2006**, *311*, 622–627.
2. Maynard, A. D.; Aitken, R. J.; Butz, T.; Colvin, V.; Donaldson, K.; Oberdorster, G.; Philbert, M. A.; Ryan, J.; Seaton, A.; Stone, V.; *et al.* Safe Handling of Nanotechnology. *Nature* **2006**, *444*, 267–269.
3. Nel, A. E.; Mädler, L.; Velegol, D.; Xia, T.; Hoek, E. M. V.; Somasundaran, P.; Klaessig, F.; Castranova, V.; Thompson, M. Understanding Biophysicochemical Interactions at the Nano-bio Interface. *Nat. Mater.* **2009**, *8*, 543–557.
4. Stasko, N. A.; Johnson, C. B.; Schoenfisch, M. H.; Johnson, T. A.; Holmuhamedov, E. L. Cytotoxicity of Polypropylenimine Dendrimer Conjugates on Cultured Endothelial Cells. *Biomacromolecules* **2007**, *8*, 3853–3859.
5. Sayes, C. M.; Fortner, J. D.; Guo, W.; Lyon, D.; Boyd, A. M.; Ausman, K. D.; Tao, Y. J.; Sitharaman, B.; Wilson, L. J.; Hughes, J. B.; *et al.* The Differential Cytotoxicity of Water-Soluble Fullerenes. *Nano Lett.* **2004**, *4*, 1881–1887.
6. Sayes, C. M.; Liang, F.; Hudson, J. L.; Mendez, J.; Guo, W.; Beach, J. M.; Moore, V. C.; Doyle, C. D.; West, J. L.; Billups, W. E.; *et al.* Functionalization Density Dependence of Single-Walled Carbon Nanotubes Cytotoxicity *in Vitro*. *Toxicol. Lett.* **2006**, *161*, 135–142.
7. Service, R. F. Nanotechnology: Can High-Speed Tests Sort out Which Nanomaterials Are Safe. *Science* **2008**, *321*, 1036–1037.
8. Abraham, V. C.; Taylor, D. L.; Haskins, J. R. High Content Screening Applied to Large-Scale Cell Biology. *Trends Biotechnol.* **2004**, *22*, 15–22.
9. Abraham, V. C.; Towne, D. L.; Waring, J. F.; Warrior, U.; Burns, D. J. Application of a High-Content Multiparameter Cytotoxicity Assay To Prioritize Compounds Based on Toxicity Potential in Humans. *J. Biomol. Screen.* **2008**, *13*, 527–537.
10. O'Brien, P. J.; Irwin, W.; Diaz, D.; Howard-Cofield, E.; Krejsa, C. M.; Slaughter, M. R.; Gao, B.; Kaludercic, N.; Angeline, A.; Bernardi, P.; *et al.* High Concordance of Drug-Induced Human Hepatotoxicity with *in Vitro* Cytotoxicity Measured in a Novel Cell-Based Model Using High Content Screening. *Arch. Toxicol.* **2006**, *80*, 580–604.
11. Jones, C. F.; Grainger, D. W. *In Vitro* Assessments of Nanomaterial Toxicity. *Adv. Drug Delivery Rev.* **2009**, *61*, 438–456.
12. Shaw, S. Y.; Westly, E. C.; Pittet, M. J.; Subramanian, A.; Schreiber, S. L.; Weissleder, R. Perturbational Profiling of Nanomaterial Biologic Activity. *Proc Natl. Acad. Sci. U.S.A.* **2008**, *105*, 7387–7392.
13. Weissleder, R.; Kelly, K.; Sun, E. Y.; Shtatland, T.; Josephson, L. Cell-Specific Targeting of Nanoparticles by Multivalent Attachment of Small Molecules. *Nat. Biotechnol.* **2005**, *23*, 1418–1423.
14. Xia, T.; Kovochich, M.; Brant, J.; Hotze, M.; Sempf, J.; Oberley, T.; Sioutas, C.; Yeh, J. I.; Wiesner, M. R.; Nel, A. E. Comparison of the Abilities of Ambient and Manufactured Nanoparticles to Induce Cellular Toxicity According to an Oxidative Stress Paradigm. *Nano Lett.* **2006**, *6*, 1794–1807.
15. Xia, T.; Kovochich, M.; Liong, M.; Mädler, L.; Gilbert, B.; Shi, H.; Yeh, J. I.; Zink, J. I.; Nel, A. E. Comparison of the Mechanism of Toxicity of Zinc Oxide and Cerium Oxide Nanoparticles Based on Dissolution and Oxidative Stress Properties. *ACS Nano* **2008**, *2*, 2121–2134.
16. Li, N.; Wang, M. Y.; Bramble, L. A.; Schmitz, D. A.; Schauer, J. J.; Sioutas, C.; Harkema, J. R.; Nel, A. E. The Adjuvant Effect of Ambient Particulate Matter is Closely Reflected by

the Particulate Oxidant Potential. *Environ. Health Perspect.* **2009**, *117*, 1116–1123.
17. Araujo, J.; Nel, A. Particulate Matter and Atherosclerosis: Role of Particle Size, Composition, and Oxidative Stress. *Part. Fibre. Toxicol.* **2009**, *6*, 24.
18. Xiao, G. G.; Wang, M.; Li, N.; Loo, J. A.; Nel, A. E. Use of Proteomics to Demonstrate a Hierarchical Oxidative Stress Response to Diesel Exhaust Particle Chemicals in a Macrophage Cell Line. *J. Biol. Chem.* **2003**, *278*, 50781–50790.
19. Li, N.; Alam, J.; Venkatesan, M. I.; Eiguren-Fernandez, A.; Schmitz, D.; Di Stefano, E.; Slaughter, N.; Killeen, E.; Wang, X.; Huang, A. Nrf2 is a Key Transcription Factor that Regulates Antioxidant Defense in Macrophages and Epithelial Cells: Protecting Against the Proinflammatory and Oxidizing Effects of Diesel Exhaust Chemicals. *J. Immunol.* **2004**, *173*, 3467–3481.
20. Xia, T.; Korge, P.; Weiss, J. N.; Li, N.; Venkatesen, M. I.; Sioutas, C.; Nel, A. Quinones and Aromatic Chemical Compounds in Particulate Matter Induce Mitochondrial Dysfunction: Implications for Ultrafine Particle Toxicity. *Environ. Health Perspect.* **2004**, *112*, 1347–1358.
21. Antonietti, Y. Z.; Antonietti, M. Synthesis of Very Small TiO_2 Nanocrystals in a Room-Temperature Ionic Liquid and Their Self-Assembly Toward Mesoporous Spherical Aggregates. *J. Am. Chem. Soc. Commun.* **2003**, *125*, 14960–14961.
22. Chen, X.; Mao, S. S. Titanium Dioxide Nanomaterials: Synthesis, Properties, Modifications, and Applications. *Chem. Rev.* **2007**, *107*, 2891–2959.
23. Niederberger, M.; Batl, M. H.; Stucky, G. D. Benzyl Alcohol and Titanium Tetrachloride- A Versatile Reaction System for the Nonaqueous and Low-Temperature Preparation of Crystalline and Luminescent Titania Nanoparticles. *Chem. Mater.* **2002**, *14*, 4364–4370.
24. Zhang, Z.; Zhong, X.; Liu, S.; Li, D.; Han, M. Aminolysis Route to Monodisperse Titania Nanorods with Tunable Aspect Ratio. *Angew Chem., Int. Ed.* **2005**, *44*, 3466–3470.
25. Qizheng, C.; Xiangting, D.; Jinxian, W.; Mei, L. Direct Fabrication of Cerium Oxide Hollow Nanofibers by Electrospinning. *J. Rare Earth* **2008**, *26*, 664–669.
26. Zhang, D.; Fu, H.; Shi, L.; Pan, C.; Li, Q.; Chu, Y.; Yu, W. Synthesis of CeO_2 Nanorods *via* Ultrasonication Assisted by Polyethylene Glycol. *Inorg. Chem.* **2007**, *46*, 2446–2451.
27. Godinho, M.; Riberio, C.; Longo, E.; Leite, E. R. Influence of Microwave Heating on the Growth of Gadolinium-Doped Cerium Oxide Nanorods. *Cryst. Growth Des.* **2008**, *8*, 384–386.
28. Feng, X.; Sayle, D. C.; Wang, Z. L.; Paras, M. S.; Santora, B.; Sutorik, A. C.; Sayle, T. X. T.; Yang, Y.; Ding, Y.; Wand, X.; *et al.* Converting Ceria Polyhedral Nanoparticles into Single Crystal Nanospheres. *Science* **2006**, *312*, 1504–1508.
29. Lee, J. S.; Kim, S. J. Synthesis and Characterization of $Ce_{1-x}Gd_xO_{2-\delta}$ Nanorods. *J. Am. Ceram. Soc.* **2007**, *90*, 661–663.
30. Karmakar, D.; MandaL, S. K.; Kadam, R. M.; Paulose, P. L.; Rajarajan, A. K.; Nath, T. K.; Das, A. K.; Dasgupta, I. Ferromagnetism in Fe-Doped ZnO Nanocrystals: Experiment and Theory. *Phys. Rev. B* **2007**, *75*, 144404–144414.
31. Xingfu, Z.; Zhaolin, H.; Yiqun, F.; Su, C.; Weiping, D.; Nanping, X. Microspheric Organization of Multilayered ZnO Nanosheets with Hierarchically Porous Structures. *J. Phys. Chem. C* **2008**, *112*, 11722–11728.
32. Height, M. J.; Mädler, L.; Pratsinis, S. E. Nanorods of ZnO Made by Flame Spray Pyrolysis. *Chem. Mater.* **2006**, *18*, 572–578.
33. Yang, D.-S.; Lao, C.; Zewail, A. H. 4D Electron Diffraction Reveals Correlated Unidirectional Behavior in Zinc Oxide Nanowires. *Science* **2008**, *321*, 1660–1664.
34. Zhengrong, R. T.; Voigt, J. A.; Liu, J.; Mckenzie, B.; Mcdermott, M. J.; Rodriguez, M. A.; Konishi, H.; Xu, H. Complex and Oriented ZnO Nanostructures. *Nat. Mater.* **2003**, *2*, 821–826.
35. Mayer, A.; Vadon, M.; Rinner, B.; Novak, A.; Wintersteiger, R.; Fröhlich, E. The Role of Nanoparticle Size in Hemocompatibility. *Toxicology* **2009**, *258*, 139–147.
36. Rezwan, K.; Studart, A. R.; Voros, J.; Gauckler, L. J. Change of ζ Potential of Biocompatible Colloidal Oxide Particles upon Adsorption of Bovine Serum Albumin and Lysozyme. *J. Phys. Chem. B* **2005**, *109*, 14469–14474.
37. Xia, T.; Kovochich, M.; Liong, M.; Zink, J. I.; Nel, A. E. Cationic Polystyrene Nanosphere Toxicity Depends on Cell-Specific Endocytic and Mitochondrial Injury Pathways. *ACS Nano* **2008**, *2*, 85–96.
38. Mädler, L.; Stark, W. J.; Pratsinis, S. E. Rapid Synthesis of Stable ZnO Quantum Dots. *J. Appl. Phys.* **2002**, *92*, 6537–6540.
39. Shailaja, M.; Kavita, B.; Bendre, B. S.; Valerie, J. L.; Subhash, H. R. Spectroscopic and Structural Characterization of Electrochemically Grown ZnO Quantum Dots. *J. Appl. Phys.* **1999**, *85*, 2861–2865.
40. Meng, H.; Xia, T.; George, S.; Nel, A. E. The Use of a Predictive Toxicological Paradigm to Study Nanomaterial Toxicity. *ACS Nano* **2009**, *3*, 1620–1627.
41. Martin, C. J.; Le, X. C.; Guidotti, T. L.; Yalcin, S.; Chum, E.; Audette, R. J.; Liang, C. K.; Yuan, B. S.; Zhang, X.; Wu, J. Zinc Exposure in Chinese Foundry Workers. *Am. J. Ind. Med.* **1999**, *35*, 574–580.
42. Rohrs, L. C. Metal-Fume Fever from Inhaling Zinc Oxide. *Arch. Inter. Med.* **1957**, *100*, 44–49.
43. Gordon, T.; Fine, J. M. Metal Fume Fever. *Occup. Med.—State Art Rev.* **1993**, *8*, 505–517.
44. Kroemer, G.; Galluzzi, L.; Vandenabeele, P.; Abrams, J.; Alnemri, E. S.; Baehrecke, E. H.; Blagosklonny, M. V.; El-Deiry, W. S.; Golstein, P.; Green, D. R.; *et al.* Classification of Cell Death: Recommendations of the Nomenclature Committee on Cell Death 2009. *Cell Death Differ.* **2008**, *16*, 3–11.
45. Perraud, A. L.; Knowles, H. M.; Schmitz, C. Novel Aspects of Signaling and Ion-Homeostasis Regulation in Immunocytes: The TRPM Ion Channels and their Potential Role in Modulating the Immune Response. *Mol. Immunol.* **2004**, *41*, 657–673.
46. Ihara, Y.; Kageyama, K.; Kondo, T. Overexpression of Calreticulin Sensitizes SERCA2a to Oxidative Stress. *Biochem. Biophys. Res. Commun.* **2005**, *329*, 1343–1349.
47. Rodriguez-Enriquez, S.; He, L.; Lemasters, J. J. Role of Mitochondrial Permeability Transition Pores in Mitochondrial Autophagy. *Int. J. Biochem. Cell Biol.* **2004**, *36*, 2463–2472.
48. Halestrap, A. P.; McStay, G. P.; Clarke, S. J. The Permeability Transition Pore Complex: Another View. *Biochimie* **2002**, *84*, 153–166.
49. Jung, E. J.; Avliyakulov, N. K.; Boontheung, P.; Loo, J. A.; Nel, A. E. Pro-oxidative DEP Chemicals Induce Heat Shock Proteins and an Unfolding Protein Response in a Bronchial Epithelial Cell Line as Determined by DIGE Analysis. *Proteomics* **2007**, *7*, 3906–3918.
50. Xia, T.; Li, N.; Nel, A. E. Potential Health Impact of Nanoparticles. *Annu. Rev. Public Health* **2009**, *30*, 137–150.
51. Godwin, H. A.; Chopra, K.; Bradley, K. A.; Cohen, Y.; Harthorn, B. H.; Hoek, E. M. V.; Holden, P.; Keller, A. A.; Lenihan, H. S.; Nisbet, R. M.; *et al.* The University of California Center for the Environmental Implications of Nanotechnology. *Environ. Sci. Technol.* **2009**, *43*, 6453–6457.
52. Kahru, A., Dubourguier, H.-C. From Ecotoxicology to Nanoecotoxicology. *Toxicology*, in press.
53. Phalen, R. F.; Oldham, M. J.; Nel, A. E. Tracheobronchial Particle Dose Considerations for *in Vitro* Toxicology Studies. *Toxicol. Sci.* **2006**, *92*, 126–132.
54. Elgersma, F.; Witkamp, G. J.; Vanrosmalen, G. M. Kinetics and Mechanism of Reductive Dissolution of Zinc Ferrite in H_2O and D_2O. *Hydrometallurgy* **1993**, *33*, 165–176.
55. Wang, R. P.; Sleight, A. W.; Subramanian, M. A. An Unusual Iron Site in Iron-Doped Zinc Oxide. *J. Solid State Chem.* **1996**, *125*, 224–227.
56. Wang, L. M.; Liao, J.-W.; Peng, Z.-A.; Lai, J.-H. Doping Effects on the Characteristics of Fe:ZnO Films: Valence Transition and Hopping Transport. *J. Electrochem. Soc.* **2009**, *156*, H138–H142.

57. Jin, J.; Li, R.; Wang, H. L.; Chen, H. N.; Liang, K.; Ma, J. T. Magnetic Fe Nanoparticle Functionalized Water-Soluble Multi-Walled Carbon Nanotubules Towards the Preparation of Sorbent for Aromatic Compounds Removal. *Chem. Commun.* **2007**, *4*, 386–388.
58. Poland, C. A.; Duffin, R.; Kinloch, I.; Maynard, A.; Wallace, W. A. H.; Seaton, A.; Stone, V.; Brown, S.; MacNee, W.; Donaldson, K. Carbon Nanotubes Introduced into the Abdominal Cavity of Mice Show Asbestos-like Pathogenicity in a Pilot Study. *Nat. Nano.* **2008**, *3*, 423–428.
59. Maädler, L.; Stark, W. J.; Pratsinis, S. E. Flame-Made Ceria Nanoparticles. *J. Mater. Res.* **2002**, *17*, 1356–1362.
60. Parkhurstand, D. L.; Appelo, C. A. J. Users's Guide to PHREEQC (Version 2). *Water-Resour. Invest. Rep.* **1999**, 99–4259.